

Curvature in the Looking-Glass: Optimal Methods to Exploit Curvature of Expectation in the Loss Landscape

Jed A. Duersch¹, Tommie A. Catanach¹, Alexander Safonov¹, Jeremy Wendt²

¹Sandia National Laboratories, Livermore, CA, USA

²Sandia National Laboratories, Albuquerque, NM, USA
 {jaduers, tacatan, amsafon, jdwendt}@sandia.gov

Abstract

Harnessing the local topography of the loss landscape is a central challenge in advanced optimization tasks. By accounting for the effect of potential parameter changes, we can alter the model more efficiently. Contrary to standard assumptions, we find that the Hessian does not always approximate loss curvature well, particularly near gradient discontinuities, which commonly arise in deep learning architectures.

We present a new conceptual framework to understand how curvature of expected changes in loss emerges in architectures with many rectified linear units. Each ReLU creates a parameter boundary that, when crossed, induces a pseudorandom gradient perturbation. Our derivations show how these discontinuities combine to form a glass-like structure, similar to amorphous solids that contain microscopic domains of strong, but random, atomic alignment. By estimating the density of the resulting gradient variations, we can bound how the loss may change with parameter movement. Our analysis includes the optimal kernel and sample distribution for approximating glass density from ordinary gradient evaluations. We also derive the optimal modification to quasi-Newton steps that incorporate both glass and Hessian terms, as well as certain exactness properties that are possible with Nesterov-accelerated gradient updates.

Our algorithm, Alice, tests these techniques to determine which curvature terms are most impactful for training a given architecture and dataset. Additional safeguards enforce stable exploitation through step bounds that expand on the functionality of Adam. These theoretical and experimental tools lay groundwork to improve future efforts (e.g., pruning and quantization) by providing new insight into the loss landscape.

1 Introduction

We present a mathematical framework to understand how distributed gradient discontinuities arise in neural networks and the effect this phenomenon has on the topography of the loss landscape. This framework opens new optimization methods to estimate and exploit these effects.

This work began with an effort to derive the optimal kernel for estimating locally-averaged linear dependence of the gradient on parameters. During testing, however, the following experiment produced unexpected results. As a consequence, we find that the Hessian is not always the next term, after the gradient, needed to approximate loss topography.

Let $\mathcal{L}(\theta)$ represent average training loss, with gradient $g(\theta)$, for a network with parameters $\theta \in \mathbb{R}^d$. We seek to

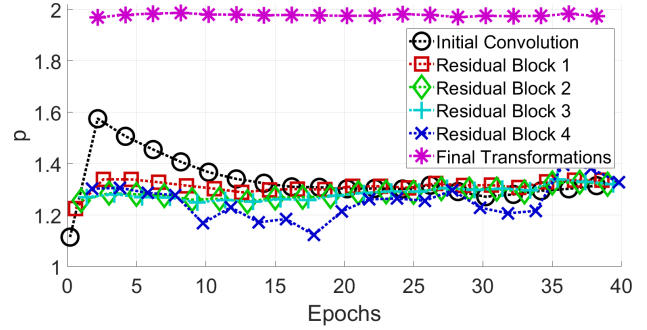


Figure 1: Exponential dependence of gradient variations on perturbations from Equation (2). A Hessian term yields $p = 2$. No low-order Taylor series can give $p < 2$.

understand how gradient changes depend on the scale of model perturbations to confirm whether a Hessian \mathbf{H} dominates. Centering parameters at $\theta = \mu$, we draw a vector of i.i.d. Rademacher samples δ (i.e. each element is equally likely to be ± 1) and then measure average gradient variations $v(\lambda)$ corresponding to a scalar distance λ as

$$v(\lambda) = \mathbb{E}[\gamma^2] \quad \text{where} \quad \gamma = g(\mu + \lambda\delta) - g(\mu). \quad (1)$$

Here, and throughout this paper, powers of vectors are applied elementwise. We use the term *gradient variations* to distinguish from variance (centered at the mean). This yields a vector of second moments centered at $g(\mu)$. By measuring gradient variations at both λ and 2λ , we can approximate a power law, $v_i(\lambda) \approx k_i \lambda^p$, over any parameter subset \mathcal{P} as

$$p(\mathcal{P}) = \log_2 \sum_{i \in \mathcal{P}} v_i(2\lambda) - \log_2 \sum_{i \in \mathcal{P}} v_i(\lambda). \quad (2)$$

If the gradient depended linearly on perturbations, i.e. $\gamma = \lambda \mathbf{H} \delta$, then Equation (2) would give $p = 2$. Figure 1 shows p for ResNet18 (He et al. 2016) with CIFAR-10 (Krizhevsky and Hinton 2009) over 40 epochs with $\lambda = 0.002$. Parameters are partitioned by: 1. initial convolutions, 2-5. each residual block, and 6. final transformations.

These results cannot be explained by a low-order truncated Taylor series, for which $p \geq 2$. Rather, these values of p suggest a balance between linear and quadratic terms in gradient variations (i.e. sublinear and linear, respectively, in

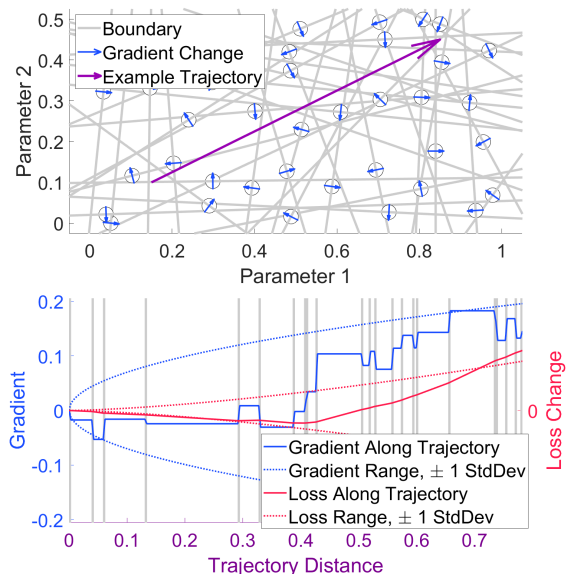


Figure 2: Illustration of gradient glass in 2D (top). Gray lines are domain boundaries due to changing a ReLU state. Blue arrows show the resulting gradient perturbations. We can compute the curvature of expected changes (bottom) to the gradient and loss from the density of these variations.

the gradient). Thus, a coherent mathematical framework to explain this phenomenon is needed.

Contributions We present an analytic framework for loss topography based upon a gradient glass structure that recovers linearity in gradient variations. The term *glass* alludes to the structure of an amorphous solid, comprising small domains of strong molecular alignment that randomly shifts at domain boundaries. Figure 2 illustrates a gradient glass in 2D (top) and the resulting loss effects, including expectation bounds (bottom). Crossing a domain boundary (gray line) results in a pseudorandom addition to the gradient (blue arrows). We can derive this structure from ReLUs in the network (Nair and Hinton 2010). The results in Figure 1 are also consistent with this explanation. Since the final parameters are not followed by ReLUs, their gradients do not encounter glass discontinuities, leaving $p = 2$ from the Hessian.

Despite the jagged effects of a gradient glass on the loss topography, we can still analyze and compute the *curvature of expectation*, including the contribution from a locally averaged Hessian, to improve loss extrapolation for various optimization tasks. Our derivations include:

1. the density of gradient variations from ReLUs,
2. the optimal kernel for estimating diagonal dependence of both the locally-averaged Hessian and glass density,
3. the optimal corresponding sample distribution,
4. upper bounds on expected changes in loss,
5. the optimal modification to quasi-Newton steps, and
6. exactness properties from Nesterov acceleration.

Although our primary contributions are theoretical, basic loss reduction is a necessary stage of development before ex-

panding to other optimization tasks. Thus, we present a simple training algorithm, Alice¹, to examine these techniques in practice and provide a baseline for further advances that leverage glass-based curvature. While well-tuned learning schedules can eventually converge to models with strong performance, rapid loss reduction can only be achieved with high-quality topographical information. Thus, Alice can reveal which curvature terms and length scales are useful for understanding a curious landscape.

Section 2 discusses related work followed by our analytic results in Section 3. Section 4 provides the implementation details used in Alice along with numerical experiments. Section 5 provides concluding remarks. Proofs are provided in Appendix A. The extended version of this paper contains additional methodological details (Appendix B) and experimental setups (Appendix C).

2 Related Work

Quasi-Newton (QN) methods use an invertible Hessian approximation to capture local curvature and attempt more efficient parameter updates, if the loss is smooth enough for the Hessian to be informative. Work incorporating curvature into ML optimization, via second-order terms, began with Becker, Le Cun et al. (1988). In multilayer perceptrons, the Hessian diagonal $\mathbf{h}(\boldsymbol{\theta})$ is directly computed by propagating second derivatives on each hidden unit. This facilitates pruning (LeCun, Denker, and Solla 1989) or improves convergence with QN steps, $\boldsymbol{\mu} \leftarrow \boldsymbol{\mu} - g(\boldsymbol{\mu}) * (|\mathbf{h}(\boldsymbol{\mu})| + \varepsilon)^{-1}$. We denote the Hadamard product with $*$.

Since then, there has been extensive work on second-order methods. Bottou, Curtis, and Nocedal (2018) provide an overview of these developments. Notably, they explain how the Hessian need not be as exact as the gradient, allowing for sub-sampled estimators (updating Hessian information less frequently or with smaller batches) to speed up optimization.

Recently, Yao et al. (2020) present methods to probe the spectrum of the Hessian for large networks. They avoid forming an explicit Hessian by using a second stage of backpropagation to obtain Hessian-vector products. If \mathbf{x} is a given vector in the product $H(\boldsymbol{\theta})\mathbf{x}$, then one computes $\nabla_{\boldsymbol{\theta}} g(\boldsymbol{\theta})^T \mathbf{x}$ after the first stage of backpropagation. Using power iteration and randomized methods, their tools provide insight into how architecture design affects optimization.

Active Developments The following summaries, by no means extensive, indicate the active interest in using curvature to advance optimization, due in part to the potential connection with generalizability. Lyle et al. (2023) examine how plasticity (a model’s ability to absorb new data) is heavily influenced by changes in loss curvature, and Kong et al. (2023) shows that catastrophic forgetting can be mitigated by controlling the maximum Hessian eigenvalue. In transfer learning, Hemati et al. (2023) forge connections between the Hessian, specifically at the classification head, and out-of-distribution transfer. Li and Spratling (2023) investigate whether curvature-based regularization can benefit adversarial training objectives. To exploit curvature, Sen, Mo-

¹<https://github.com/sandialabs/alice>

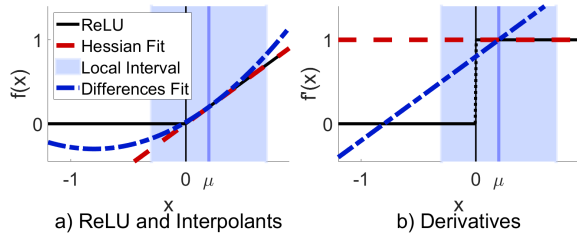


Figure 3: ReLU extrapolation. Hessian fitting cannot account for gradient discontinuities, whereas curvature matching gradient changes provides a better fit on a local interval.

han, and Qin (2023) use diagonal Hessian approximations to improve convergence of federated, data-parallel, training. Kaur, Cohen, and Lipton (2023) analyze the relationship between curvature and generalization, showing how that the largest Hessian eigenvalues can be controlled through batch size and learning rate adjustments in Sharpness-Aware Minimization (SAM). Lee, Yoo, and Kwak (2023) also present an algorithm to suppress Hessian curvature along optimization pathways, and Lee, He, and Avestimehr (2023) use learning rate adjustments to encourage convergence at flat minima. Duersch (2024) provides a method to merge QN with variational inference, showing how the Hessian diagonal can calibrate model uncertainty while improving parameter updates.

Our derivations also include a variation of Nesterov accelerated quasi-Newton (NAQ), initially proposed by Ninomiya (2017) and Indrapriyadarsini et al. (2020). They combine QN methods with Nesterov acceleration, focusing on the symmetric low-rank Hessian updates of Broyden-Fletcher-Goldfarb-Shanno (BFGS) methods. The cost of these methods scales linearly with approximation rank, which can be prohibitive for very large architectures. See (Nocedal and Wright 2006) for details regarding BFGS.

Hessian Shortcomings Despite the many successes of Hessian-based approaches, the resulting interpolants are not always the best way to approximate local curvature, particularly in the vicinity of gradient discontinuities.

Figure 3 illustrates this issue with a basic ReLU, $f(x) = \max(0, x)$. Curvature matching the difference of gradients follows local changes and anticipates gradient zeros, whereas the Hessian fails to obtain any curvature that could inform optimization. Work by Frumkin, Gope, and Marculescu (2023), regarding how to account for the jagged loss topography they observe during quantization, also supports this picture of loss topography. Moreover, Li, Li, and Zhan (2024) find that loss typically has v-shaped structure along random trajectories, which bears a critical connection to a predicate in our Theorem 4 (See Section 3), that random loss trajectories are reflected at a local floor.

Glass in the Literature Glasses are technically physical systems with non-convex energy functions of state. There have been a few papers referencing a notion of a glass with respect to high-dimensional optimization problems. Dauphin et al. (2014) provide both analytic and experimental evidence for a proliferation of saddle points, rather

than local minima, as model dimensionality increases. This perspective draws insight from spin-glasses in statistical physics (Parisi 2007). Saddle points are critical points (gradient zeros) where \mathbf{H} contains both positive and negative eigenvalues. In the vicinity of such points, low apparent curvature creates an illusion of convergence, despite the hidden potential to make progress. To address this problem, they support saddle-free Newton, which repels saddle points by using $|\mathbf{H}|$, the rectified matrix constructed from absolute values of Hessian eigenvalues (Nocedal and Wright 2006).

Choromanska et al. (2015) go on to show that, while many local minima may also exist, large networks provide high probability of convergence to solutions of similar performance, with local minima of poor quality becoming increasingly rare. Spigler et al. (2019) also establish a connection between glasses and the phase transition in generalizability as deep networks change from under- to over-parameterization. They show how the phenomenon of overfitting is most problematic in the vicinity of this transition.

The distribution of critical points in the loss topography directly arises from the gradient variations that we scrutinize. Our objective is to lay groundwork for simple and computationally efficient methods to navigate the resulting topography to support novel optimization tasks.

3 Derivations

Theorem 1 relates discontinuities in ReLU derivatives to the loss' gradient discontinuities. See Appendix A for proofs.

Theorem 1 (Glass from ReLUs) Consider a network with many ReLUs. Let a single unit be $z = \max(y, 0) \in \mathbb{R}$. To examine the effect of a small parameter perturbation, $\theta = \mu + \delta$, on the gradient variations defined by Equation (1), we hold network inputs fixed and assume each ReLU input is locally linearly dependent on the perturbation,

$$y(\mu + \delta) = y(\mu) + \delta^T \hat{\gamma} \quad \text{where} \quad \hat{\gamma} = \nabla_{\mu} y(\mu). \quad (3)$$

Suppose a subset of ReLUs have pre-activation values that are uniformly distributed at random in an interval $[-\psi, \psi]$, indexed by $\mathcal{S}_{\psi} = \{k \mid z^{(k)} = \max(y^{(k)}, 0), |y^{(k)}| < \psi\}$, and perturbations satisfy $|\delta^T \hat{\gamma}^{(k)}| < \psi$. Then, treating the pre-activation gradients $\hat{\gamma}^{(k)}$ as independent zero-mean pseudorandom variables, the gradient variations are bound by $\mathbf{v}(\delta) \leq \mathbf{R}|\delta|$ where \mathbf{R} is a matrix with elements

$$\mathbf{R}_{ij} = \frac{1}{2\psi} \sum_{k \in \mathcal{S}_{\psi}} \hat{\gamma}_i^{(k)2} \left(\frac{d\mathcal{L}(\mu)}{dz^{(k)}} \right)^2 |\hat{\gamma}_j^{(k)}|. \quad (4)$$

We interpret \mathbf{R} as a density matrix that captures additional gradient variations per unit length. Any activation function with ReLU-like discontinuities in the derivative will induce discontinuities in the loss gradient. The same reasoning holds for activation functions with rapidly changing derivatives that can be approximated by a step function. Although Theorem 1 is restricted to a fixed input, if we consider a full dataset, averaging diminishes the size of individual discontinuities, but they still remain. Critically, point-wise Hessian methods cannot detect their presence or effects.

Note the dependence of \mathbf{R}_{ii} on $|\gamma_i^{(k)}|^3$. The largest magnitude element, $|\gamma_{i_{\max}}^{(k)}| > |\gamma_j^{(k)}|$ for all $j \neq i_{\max}$, has a much stronger diagonal effect, $|\gamma_{i_{\max}}^{(k)}|^3 > |\gamma_{i_{\max}}^{(k)}|^2 |\gamma_j^{(k)}| > |\gamma_j^{(k)}|^2 |\gamma_{i_{\max}}^{(k)}|$. Since the largest element differs over the various $k \in \mathcal{S}_\psi$, these dominant terms are distributed over many diagonal elements. Thus, taking $\mathbf{v} \approx \boldsymbol{\rho} * |\boldsymbol{\delta}|$, where $\boldsymbol{\rho} = \text{diag}(\mathbf{R})$, is a simple and reasonable approximation.

Theorem 2 estimates the diagonal of linear operators by sampling matrix-vector multiplies, allowing both $\boldsymbol{\rho}$ and \mathbf{h} , the diagonal of the locally averaged Hessian, to be computed from ordinary gradients evaluated at sample locations.

Theorem 2 (Optimal Kernel for Estimating Diagonal)

We are given a probability density over perturbations $p(\boldsymbol{\delta})$ as a product of i.i.d. factors, $p(\boldsymbol{\delta}) = \prod_{i=1}^d p(\delta_i)$, each having zero mean and unit variance. If we have a mechanism to evaluate matrix-vector products, $\mathbf{y} = \mathbf{M}\boldsymbol{\delta}$, then we can estimate each element \mathbf{m}_i of the diagonal $\mathbf{m} = \text{diag}(\mathbf{M})$ using samples weighted by a kernel function of the corresponding sample element $\kappa_i(\delta_i)$:

$$\mathbb{E}[\kappa_i(\delta_i)\mathbf{y}_i] = \int \kappa_i(\delta_i)\mathbf{y}_i dp(\boldsymbol{\delta}) = \mathbf{m}_i. \quad (5)$$

If off-diagonal elements scale as $\sum_{j \neq i} \mathbf{M}_{ij}^2 = \omega_i^2 \mathbf{m}_i^2$ for $i \in [d]$, then the zero-bias minimum-variance kernel is

$$\kappa_i^*(\delta_i) = \frac{c^{-1}\delta_i}{\delta_i^2 + \omega_i^2} \quad \text{where} \quad c = \int \frac{\delta_i^2}{\delta_i^2 + \omega_i^2} dp(\delta_i). \quad (6)$$

Theorem 2 applies to any sample density with i.i.d. factors that have zero mean and unit variance, but it requires knowing the scaling factor ω_i^2 for off-diagonal matrix elements. Fortunately, the optimal distribution in Theorem 3 obviates this issue. Otherwise, it can be proven that $\omega_i^2 \leq 1$ for diagonally dominant matrices, providing a conservative choice.

See Appendix B for a note regarding restricted updates, which further reduce estimation errors by hollowing out the update density. Consistently, Theorem 3 shows that the optimal density removes all small perturbations.

Theorem 3 (Optimal Perturbation Density) *From the set of perturbation densities that comprise a product of i.i.d. factors, $p(\boldsymbol{\delta}) = \prod_{i=1}^d p(\delta_i)$, with zero mean and unit variance in each coordinate, the optimal density to minimize the estimator variance in Theorem 2 is the Rademacher distribution in each factor, i.e. $\frac{1}{2}$ probability of either -1 or 1 . Then, Equation (6) gives $\kappa_i^*(\delta_i) = \delta_i$.*

Given optimal mechanisms to approximate the density of gradient variations, we derive an upper bound on expected increases in loss. The bound in Theorem 4 follows from an assertion that predictive loss cannot become arbitrarily negative. Rather, reductions due to small parameter changes are bound from below by a *local floor*, the minimum loss that can be reached by a small change to a single parameter.

Theorem 4 (Curvature of Expectation in Glass Loss)

As we displace parameters by $\boldsymbol{\delta}$, the increase in loss $\Delta\mathcal{L}(\boldsymbol{\delta}) = \mathcal{L}(\boldsymbol{\mu} + \boldsymbol{\delta}) - \mathcal{L}(\boldsymbol{\mu})$ is greatest if a local floor enforces $\Delta\mathcal{L}(\delta_k) \geq 0$. Using the diagonal approximation

of gradient variations, $\mathbf{v} \approx \boldsymbol{\rho} * |\boldsymbol{\delta}|$ with $\boldsymbol{\rho} \succcurlyeq 0$, and treating corresponding loss effects independently in each coordinate, we obtain the upper bound on expected increases in loss

$$\mathbb{E}[\Delta\mathcal{L}(\boldsymbol{\delta})] \leq \sqrt{\frac{2}{3\pi}} \boldsymbol{\rho}^{\frac{1}{2}T} |\boldsymbol{\delta}|^{\frac{3}{2}}. \quad (7)$$

Theorems 2 and 3 are useful even when a glass term is not needed, since the resulting \mathbf{h} accounts for distributed gradient changes that hold over a larger scale. When present, the additional curvature due to Theorem 4 reduces the length of an optimal step. Theorem 5 incorporates this additional curvature into QN steps that also include a non-negative \mathbf{h} .

Theorem 5 (Optimal Modification to Quasi-Newton) *By combining the bound in Equation (7) with the gradient \mathbf{g} and a nonnegative Hessian diagonal $\mathbf{h} \succcurlyeq 0$, so that*

$$\mathcal{L}(\boldsymbol{\mu} + \boldsymbol{\delta}) \leq \mathcal{L}(\boldsymbol{\mu}) + \boldsymbol{\delta}^T \left(\mathbf{g} + \frac{1}{2} \mathbf{h} * \boldsymbol{\delta} \right) + \sqrt{\frac{2}{3\pi}} \boldsymbol{\rho}^T |\boldsymbol{\delta}|^3,$$

the minimizer is $\boldsymbol{\delta} = -\mathbf{g} * \bar{\mathbf{h}}^{-1}$ using the modified Hessian

$$\bar{\mathbf{h}} = \hat{\mathbf{h}} + \mathbf{h} + \sqrt{\hat{\mathbf{h}} * (\hat{\mathbf{h}} + 2\mathbf{h})} + \varepsilon \quad \text{where} \quad (8)$$

$$\hat{\mathbf{h}} = 3\boldsymbol{\rho} * (4\pi|g(\boldsymbol{\mu})| + \varepsilon)^{-1}. \quad (9)$$

We have added $\varepsilon > 0$ terms for numerical stability.

Unfortunately, a simple example shows that QN steps are often too greedy, especially for over-parameterized models: take an underdetermined linear system comprising a random matrix $\mathbf{A} \in \mathbb{R}^{10 \times 100}$ and vector $\mathbf{b} \in \mathbb{R}^{10 \times 1}$. For $\mathbf{x} \in \mathbb{R}^{100}$, let the loss be $\mathcal{L}(\mathbf{x}) = \frac{1}{2} \|\mathbf{A}\mathbf{x} - \mathbf{b}\|_2^2$ with gradient $g(\mathbf{x}) = \mathbf{A}^T(\mathbf{A}\mathbf{x} - \mathbf{b})$ and Hessian diagonal $\mathbf{h} = \text{diag}(\mathbf{A}^T \mathbf{A})$. In an actual (first) trial, a QN step from zero gave $\|\mathbf{x}\|_2 = 3.75$ with an *increase* in loss from 5.6 to 464.6. The minimal solution needed only $\|\mathbf{x}_{\min}\|_2 = 1.1$, showing off-diagonal terms' importance. Fortunately, damped QN steps solve this problem; only one 10% step reduced the loss to 0.8.

Nesterov Accelerated Quasi-Newton Damped QN steps create an opportunity to not only reduce the loss more efficiently, but also improve the correctness of gradient updates with NAQ. The approaches taken by Ninomiya (2017) and Indrapriyadarsini et al. (2020) scale QN steps with an Armijo line search, but we show how a simple relationship with the gradient momentum coefficient, β_1 in Adam (Kingma and Ba 2014), provides desirable exactness properties. To understand this, we briefly review some related optimization practices. See Ruder (2016) for an overview.

Nesterov acceleration anticipates gradient changes by distinguishing the actual state of an optimization trajectory from the location of gradient evaluations. In our notation, at step s we have a tentative parameter update $\boldsymbol{\delta}^{(s)}$. The actual parameter position $\boldsymbol{\mu}^{(s)}$ will be updated by taking a fraction $\varphi \leq 1$ of the full step, but the next gradient will be evaluated at a new location $\boldsymbol{\nu}^{(s+1)}$ with a different factor $\omega \geq \varphi$:

$$\boldsymbol{\mu}^{(s+1)} = \boldsymbol{\mu}^{(s)} + \varphi \boldsymbol{\delta}^{(s)} \quad \text{vs} \quad \boldsymbol{\nu}^{(s+1)} = \boldsymbol{\mu}^{(s)} + \omega \boldsymbol{\delta}^{(s)}. \quad (10)$$

These updates combine with gradient momentum as

$$\mathbf{g}^{(s+1)} = \beta_1 \mathbf{g}^{(s)} + (1 - \beta_1) \mathbf{g}(\boldsymbol{\nu}^{(s)}). \quad (11)$$

Going forward, we use the modified Hessian $\bar{\mathbf{h}}$ from Equation (8) with the quadratic loss approximation

$$\mathcal{L}(\boldsymbol{\mu}^{(s)} + \boldsymbol{\delta}) = \mathcal{L}(\boldsymbol{\mu}^{(s)}) + \boldsymbol{\delta}^T \left(\mathbf{g}^{(s)} + \bar{\mathbf{h}} * \boldsymbol{\delta} / 2 \right), \quad (12)$$

which matches the gradient at $\boldsymbol{\mu}$ while keeping the optimal step. With this setup, Theorem 6 shows how certain φ and ω yield exactness properties in Equation (11).

Theorem 6 (Exact Nesterov Accelerated Quasi-Newton)
For the purpose of optimization, we apply the loss approximation in Equation (12) with the matching gradient

$$\mathbf{g}(\boldsymbol{\mu}^{(s)} + \boldsymbol{\delta}) = \mathbf{g}^{(s)} + \bar{\mathbf{h}} * \boldsymbol{\delta}, \quad (13)$$

and optimal step, $\boldsymbol{\delta}^{(s)} = -\mathbf{g}^{(s)} * \bar{\mathbf{h}}^{-1}$. Yet, suppose the true gradient has unknown linear dependence

$$\mathbf{g}^*(\boldsymbol{\mu}^{(s)} + \boldsymbol{\delta}) = \mathbf{g}^*(\boldsymbol{\mu}^{(s)}) + \mathbf{H}\boldsymbol{\delta} \quad (14)$$

that holds through displacements to $\boldsymbol{\delta}^{(s)}$, our projected optimum. Then, the Nesterov acceleration coefficients,

$$\varphi = 1 - \beta_1 \quad \text{and} \quad \omega = 1, \quad (15)$$

ensure that the running gradient reduction by β_1 in Equation (11) matches Equation (13) and the new gradient evaluation exactly captures the unknown linear dependence in Equation (14), while suppressing errors $\boldsymbol{\gamma}^{(s)}$ so that

$$\begin{aligned} \mathbf{g}^{(s)} &= \mathbf{g}^*(\boldsymbol{\mu}^{(s)}) + \boldsymbol{\gamma}^{(s)} \quad \text{goes to} \\ \mathbf{g}^{(s+1)} &= \mathbf{g}^*(\boldsymbol{\mu}^{(s+1)}) + \beta_1 \boldsymbol{\gamma}^{(s)}. \end{aligned} \quad (16)$$

Theorem 6 provides updates that capture hidden linear discrepancies (diagonal and off-diagonal) averaged over the distance to the optimum we anticipate from our current knowledge. Since the gradient damping is consistent with our loss topography estimate, the following methods extinguish gradient information at the same rate it is exploited.

4 Methods and Experiments

Alice allows us to study which curvature computations are most suitable for capturing an architecture’s loss topography, with follow-on implications for sensitivity-based pruning and quantization. By showing the impact that these curvature computations have on early training, Alice identifies what is needed for longer or more complex procedures.

To compute three parameter-length quantities \mathbf{g} , $\boldsymbol{\rho}$, and \mathbf{h} , we need three gradient evaluations. To be consistent with Equation (10), these are anchored to $\boldsymbol{\nu}$ rather than $\boldsymbol{\mu}$:

$$\mathbf{g}^{(+)} = \mathbf{g}(\boldsymbol{\nu} + \lambda \boldsymbol{\delta}) = \mathbf{g}(\boldsymbol{\nu}) + \lambda \mathbf{H}\boldsymbol{\delta} + \boldsymbol{\gamma}^{(+)} \quad (17)$$

$$\mathbf{g}^{(-)} = \mathbf{g}(\boldsymbol{\nu} - \lambda \boldsymbol{\delta}) = \mathbf{g}(\boldsymbol{\nu}) - \lambda \mathbf{H}\boldsymbol{\delta} + \boldsymbol{\gamma}^{(-)}, \quad \text{and} \quad (18)$$

$$\mathbf{g}^{(0)} = \mathbf{g}(\boldsymbol{\nu}). \quad (19)$$

Algorithm 1: Alice Topography Update

Input: evaluation center: $\boldsymbol{\nu}$; gradient function: $\mathbf{g}(\boldsymbol{\theta})$.
Input and Output: running averages: \mathbf{g} , $\boldsymbol{\rho}$, and \mathbf{h} .
Hyperparameters: $\lambda, \beta_1, \beta_2$.

- 1: Draw Rademacher t .
- 2: Evaluate $\mathbf{g}^{(\pm)} = \mathbf{g}(\boldsymbol{\nu} \pm \lambda t)$ and $\mathbf{g}^{(0)} = \mathbf{g}(\boldsymbol{\theta})$.
- 3: $\mathbf{g} \leftarrow \beta_1 \mathbf{g} + (1 - \beta_1) \mathbf{g}^{(0)}$.
- 4: $\mathbf{h} \leftarrow \beta_2 \mathbf{h} + (1 - \beta_2) \frac{1}{2\lambda} |\mathbf{g}^{(+)} - \mathbf{g}^{(-)}|$.
- 5: $\boldsymbol{\rho} \leftarrow \beta_2 \boldsymbol{\rho} + (1 - \beta_2) \frac{2}{\lambda} \left(\frac{1}{2} (\mathbf{g}^{(+)} + \mathbf{g}^{(-)}) - \mathbf{g}^{(0)} \right)^2$.

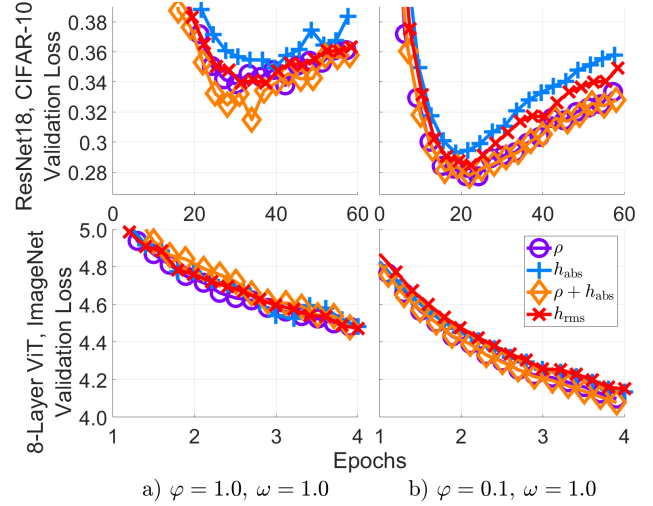


Figure 4: Alice training with various curvature terms: a) full QN steps, b) NAQ steps (Theorem 6).

These expressions capture average linear dependencies as matrix-vector multiplies, $\mathbf{H}\boldsymbol{\delta}$. Similarly, the gradient perturbations $\boldsymbol{\gamma}^{(\pm)}$ reveal glass density $\mathbb{E}[\boldsymbol{\gamma}^{(\pm)2}] = \mathbf{R}|\boldsymbol{\delta}|$:

$$\mathbf{H}\boldsymbol{\delta} = \mathbb{E} \left[\left(\mathbf{g}^{(+)} - \mathbf{g}^{(-)} \right) / (2\lambda) \right], \quad \text{and} \quad (20)$$

$$\mathbf{R}|\boldsymbol{\delta}| = \mathbb{E} \left[\left(\left(\mathbf{g}^{(+)} + \mathbf{g}^{(-)} \right) / 2 - \mathbf{g}^{(0)} \right)^2 / (2\lambda) \right]. \quad (21)$$

We can apply Theorem 3 without storing $\boldsymbol{\delta}$ by enforcing non-negative \mathbf{h} , since $|\boldsymbol{\delta} * \mathbf{H}\boldsymbol{\delta}| = |\mathbf{H}\boldsymbol{\delta}|$, which also repels saddle points. Algorithm 1 shows how we incorporate these evaluations into running topography updates.

Alice can also enable quick-steps that avoid updating the Hessian and glass densities too often. For example, taking 3 regular steps (1 gradient each) between every full step (3 gradients) reduces costs to 6 gradients every 4 steps (i.e. half of full extraction on every step). The optimization impact can be small in comparison to speed improvements.

Nesterov Acceleration Figure 4 examines the efficacy of NAQ with various curvature terms: \mathbf{h}_{abs} is $|\mathbf{h}|$ (Algorithm 1, Line 4) and $\boldsymbol{\rho}$ indicates glass density (Line 5). We also include an RMS version \mathbf{h}_{rms} that is similar to AdaHessian (Yao et al. 2021). Our ViT model uses a linear-complexity form of attention (Shen et al. 2021) trained with the 64 ×

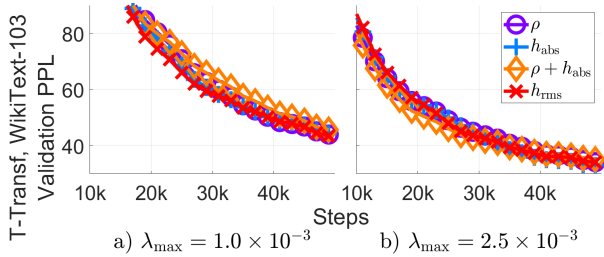


Figure 5: Training effect of increased exploitation bound.

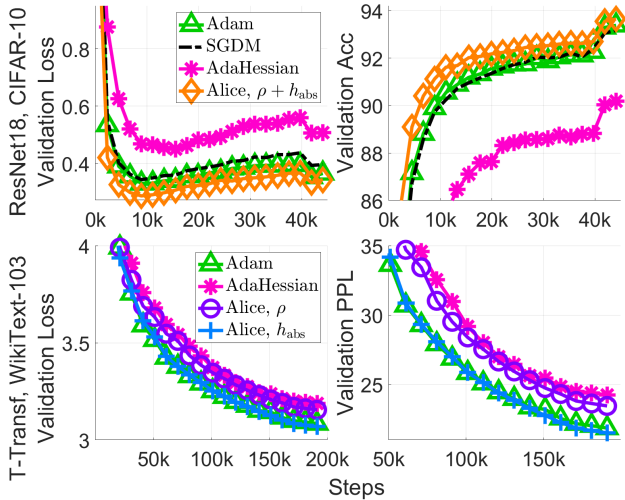


Figure 6: Optimization method comparisons.

64 downsampled Imagenet (Deng et al. 2009; Chrabaszcz, Loshchilov, and Hutter 2017). The first column shows full QN steps, and the second employs the NAQ coefficients in Equation (15). Both NAQ and curvature using glass terms yield the best results.

Exploration and Stability In principle, tracking loss curvature does not preclude traps (e.g., local minima or flat saddle points) from blocking progress. Moreover, Theorem 5’s optimal step can become very large and exceed trustworthy extrapolation. Alice addresses these problems using learning rate bounds λ_{\min} and λ_{\max} that can be interpreted as: 1. fixed step lengths, 2. SGD-M learning rates, or 3. Adam learning rates. Between these bounds, Alice takes NAQ steps. This simple approach ensures that updates exploiting curvature remain sufficiently large and stable.

Figure 5 shows the importance of stability limits for early loss reduction using the Tensorised Transformer (Ma et al. 2019) with the WikiText-103 corpus (Merity et al. 2016) and Adam-based bounds. Here, increasing λ_{\max} offers a clear benefit. Conveniently, by setting $\varphi = \omega = 1$ and $\lambda_{\min} = \lambda_{\max} = \text{learn-rate}$, Alice replicates either SGD-M or Adam. Thus, Alice can always perform at least as well as these methods, and further adjustments offer a possibility of improvement.

Method Comparisons Although our aim is to lay groundwork for additional optimization challenges, we include some comparisons against related optimizers for basic loss reduction with dense parameters. Figure 6 shows validation quality on ResNet18 trained with stochastic gradient descent with momentum (SGD-M), Adam, Adahessian, and Alice.

5 Summary

Summary We developed a mathematical framework to understand the influence of dense gradient discontinuities on the loss topography. These discontinuities are caused by ReLU-like activation functions, which form a gradient glass when they occur in high numbers. We then derived the optimal kernel and sample density for estimating locally-averaged diagonal dependencies from matrix-vector products, allowing us to approximate linear gradient dependence (i.e., the locally-averaged Hessian diagonal) and gradient variations (i.e., the local glass density) from ordinary back-propagation. We also showed how expected changes in the loss are bound by a $\frac{3}{2}$ power law.

By including glass terms in the loss, we derived the optimal modification to quasi-Newton steps to unify model updates in architectures that may have gradient effects that are dominated by either term. Further, our analysis of Nesterov acceleration finds that certain coefficients can exactly capture the gradient reductions we expect, while also correcting hidden linear terms in updates to a running gradient average.

Alice provides a baseline to show how these techniques can improve basic loss reduction. By examining the efficacy of different curvature approximations, we gain insight into the loss landscape that will support advanced optimization and regularization strategies currently being explored.

A Proofs

Proof of Theorem 1 W.l.o.g., consider an inactive unit at $\theta = \mu$, i.e. $y(\mu) < 0$ so that $z(\mu) = 0$. Using Equation (3) to compute the perturbation needed to cross the activation threshold gives $\delta^T \hat{\gamma} \geq -y$. This changes $\frac{\partial z}{\partial y}$ from 0 to 1, so the chain rule gives a gradient perturbation $\gamma \approx \frac{d\mathcal{L}(\mu)}{dz} \hat{\gamma}$ in Equation (1). Crossing in reverse yields a minus sign. Thus, each ReLU generates a half-space containing an additive gradient perturbation. When δ crosses the threshold (in either direction), γ^2 is added to the gradient variations.

We only need to consider these effects for ReLUs in \mathcal{S}_ψ , which have small enough inputs to potentially flip. Since $y^{(k)}$ are distributed uniformly at random over $[-\psi, \psi]$ for $k \in \mathcal{S}_\psi$, the probability that a specific δ is in the correct direction and large enough to cross the threshold is $p\left(-\text{sign}(y^{(k)})\delta^T \hat{\gamma}^{(k)} > |y^{(k)}|\right) = \frac{|\delta^T \hat{\gamma}^{(k)}|}{2\psi}$.

Treating these $\hat{\gamma}$ as independent mean zero pseudorandom variables, v is the diagonal of the variance of the sum over all resulting γ perturbations, which is just the sum of individual variances. Using the triangle inequality, $|\delta^T \hat{\gamma}^{(k)}| \leq$

$\sum_{j=1}^d |\hat{\gamma}_j^{(k)} \delta_j|$, the total variance is

$$v(\boldsymbol{\delta}) \leq \frac{1}{2\psi} \sum_{k \in \mathcal{S}_\psi} \hat{\gamma}^{(k)2} \left(\frac{d\mathcal{L}(\boldsymbol{\mu})}{dz^{(k)}} \right)^2 \sum_{j=1}^d |\hat{\gamma}_j^{(k)}| |\delta_j| \blacksquare$$

Proof of Theorem 2 We first note the elementwise expressions for matrix-vector products: $\mathbf{y}_i = \sum_j \mathbf{M}_{ij} \boldsymbol{\delta}_j$ and

$$\mathbf{y}_i^2 = \sum_j [\mathbf{M}_{ij}^2 \boldsymbol{\delta}_j^2 + \sum_{k \neq j} \mathbf{M}_{ij} \mathbf{M}_{ik} \boldsymbol{\delta}_j \boldsymbol{\delta}_k].$$

As each density $p(\boldsymbol{\delta}_j)$ has mean zero and unit variance, we obtain the following integrals over all coordinates except $\boldsymbol{\delta}_i$:

$$\int \{\mathbf{y}_i, \mathbf{y}_i^2\} \prod_{j \neq i} dp(\boldsymbol{\delta}_j) = \{\mathbf{m}_i \boldsymbol{\delta}_i, \mathbf{m}_i^2 (\boldsymbol{\delta}_i^2 + \boldsymbol{\omega}_i^2)\}. \quad (22)$$

Let $\eta(\boldsymbol{\delta}_i)$ be arbitrary feasible kernel variations near $\kappa_i^*(\boldsymbol{\delta}_i)$ as $\kappa_i(\boldsymbol{\delta}_i) = \kappa_i^*(\boldsymbol{\delta}_i) + \varepsilon \eta(\boldsymbol{\delta}_i)$, where ε is a scalar differential element. Differentiating w.r.t. to ε yields Gâteaux derivatives in any direction $\eta(\boldsymbol{\delta}_i)$. To obtain an estimator with zero bias, all feasible kernels must satisfy Equation (5). Thus,

$$\frac{\partial}{\partial \varepsilon} \int \kappa_i(\boldsymbol{\delta}_i) \mathbf{y}_i dp(\boldsymbol{\delta}) = \mathbf{m}_i \int \eta(\boldsymbol{\delta}_i) \boldsymbol{\delta}_i dp(\boldsymbol{\delta}_i) = 0. \quad (23)$$

Combining Equation (22) with the estimator variance gives

$$\begin{aligned} V &= \int [\kappa_i(\boldsymbol{\delta}_i) \mathbf{y}_i - \mathbf{m}_i]^2 dp(\boldsymbol{\delta}) = \int \kappa_i^2(\boldsymbol{\delta}_i) \mathbf{y}_i^2 dp(\boldsymbol{\delta}) - \mathbf{m}_i^2 \\ &= \mathbf{m}_i^2 \left[\int \kappa_i^2(\boldsymbol{\delta}_i) (\boldsymbol{\delta}_i^2 + \boldsymbol{\omega}_i^2) dp(\boldsymbol{\delta}_i) - 1 \right]. \end{aligned} \quad (24)$$

We can minimize V by applying the variational principle

$$\frac{\partial V}{\partial \varepsilon} = 2\mathbf{m}_i^2 \int \eta(\boldsymbol{\delta}_i) \kappa_i^*(\boldsymbol{\delta}_i) (\boldsymbol{\delta}_i^2 + \boldsymbol{\omega}_i^2) dp(\boldsymbol{\delta}_i) = 0.$$

This must hold for all feasible $\eta(\cdot)$ in Equation (23), thus $\kappa_i^*(\boldsymbol{\delta}_i) (\boldsymbol{\delta}_i^2 + \boldsymbol{\omega}_i^2) \propto \boldsymbol{\delta}_i$. Solving Equation (5) for the constant of proportionality c gives the stated result \blacksquare

Proof of Theorem 3 To apply the variational principle, we write arbitrary density perturbations $\eta(\boldsymbol{\delta}_i)$ in the vicinity of the optimizer $p^*(\boldsymbol{\delta}_i)$ as $p(\boldsymbol{\delta}_i) = p^*(\boldsymbol{\delta}_i) + \varepsilon \eta(\boldsymbol{\delta}_i)$. Since the variational principle need not hold for degrees of freedom on the boundary of the feasible set, we will enforce the restriction $\eta(\boldsymbol{\delta}_i) = 0$ when $p^*(\boldsymbol{\delta}_i) = 0$. If we only allow density perturbations that preserve normalization, we obtain

$$\frac{\partial}{\partial \varepsilon} \int dp(\boldsymbol{\delta}_i) = \frac{\partial}{\partial \varepsilon} 1 = \int d\eta(\boldsymbol{\delta}_i) = 0. \quad (25)$$

Unpacking the estimator variance, Equation (24), with the optimal kernel, Equation (6), gives

$$\mathbf{m}_i^{-2} V = \int \kappa_i^{*2}(\boldsymbol{\delta}_i) (\boldsymbol{\delta}_i^2 + \boldsymbol{\omega}_i^2) dp(\boldsymbol{\delta}_i) - 1 = c^{-1} - 1.$$

As c is a function of $p(\cdot)$, differentiating w.r.t. ε reveals the optimizer condition:

$$\mathbf{m}_i^{-2} \frac{\partial V}{\partial \varepsilon} = -c^{-2} \int \frac{\boldsymbol{\delta}_i^2}{\boldsymbol{\delta}_i^2 + \boldsymbol{\omega}_i^2} d\eta(\boldsymbol{\delta}_i) = 0.$$

This requires $\frac{\boldsymbol{\delta}_i^2}{\boldsymbol{\delta}_i^2 + \boldsymbol{\omega}_i^2}$ to be a constant when $p^*(\boldsymbol{\delta}_i) > 0$, since Equation (25) provides the only constraint on feasible $\eta(\cdot)$ on this set. Thus, only $\boldsymbol{\delta}_i = \pm x$ for some $x \geq 0$ can map to nonzero density. Solving for zero mean and unit variance gives the Rademacher distribution \blacksquare

Proof of Theorem 4 To approximate the loss effects due to movement, $\boldsymbol{\theta}_k = \boldsymbol{\mu}_k + \boldsymbol{\delta}_k$, we need to aggregate the effects of discrete gradient perturbations. If we consider n zero mean i.i.d. $\gamma_k^{(j)}$ for $j = 1, \dots, n$, that activate at equally-spaced locations $\frac{j}{n} \boldsymbol{\delta}_k$, then we have $\mathbb{E}[\gamma_k^{(j)2}] = \frac{\boldsymbol{\rho}_k |\boldsymbol{\delta}_k|}{n}$ to preserve the density $\boldsymbol{\rho}_k$. Let $\Delta_n(\boldsymbol{\delta}_k)$ represent corresponding loss changes in the absence of a local floor. Integration gives

$$\Delta_n(\boldsymbol{\delta}_k) = \sum_{j=1}^n \int_{\frac{j\boldsymbol{\delta}_k}{n}}^{\boldsymbol{\delta}_k} \gamma_k^{(j)} d\boldsymbol{\theta}_k = \sum_{j=1}^n \frac{n-j}{n} \gamma_k^{(j)} \boldsymbol{\delta}_k.$$

Since each term has zero mean, the variance is the sum. Thus

$$\mathbb{E}[\Delta_n(\boldsymbol{\delta}_k)^2] = \sum_{j=1}^n \frac{(n-j)^2}{n^2} \frac{\boldsymbol{\rho}_k |\boldsymbol{\delta}_k|}{n} \boldsymbol{\delta}_k^2 \quad \text{so}$$

$$\mathbb{E}[\Delta(\boldsymbol{\delta}_k)^2] = \lim_{n \rightarrow \infty} \frac{n - 3n^2 + 2n^3}{6n^3} \boldsymbol{\rho}_k |\boldsymbol{\delta}_k|^3 = \frac{\boldsymbol{\rho}_k |\boldsymbol{\delta}_k|^3}{3}.$$

This finite limit satisfies the Lyapunov formulation of the central limit theorem. Thus, summing variance contributions gives $\Delta(\boldsymbol{\delta}_k) \sim \mathcal{N}(0, \boldsymbol{\rho}^T |\boldsymbol{\delta}|^3 / 3)$.

We enforce the local floor $\Delta \mathcal{L}(\boldsymbol{\delta}_k) \geq 0$ by mapping every virtual loss trajectory that could be realized by $\Delta(\boldsymbol{\delta}_k)$ to a bounded trajectory $\Delta \mathcal{L}(\boldsymbol{\delta}_k) = |\Delta(\boldsymbol{\delta}_k)|$. The stated result follows from $\int |x| d\mathcal{N}(x | 0, \lambda^2) = \sqrt{\frac{2}{\pi}} \lambda^2 \blacksquare$

Proof of Theorem 5 We examine each step coordinate $\boldsymbol{\delta}_k$ independently, since the effects are just added. We can apply the variational principle by differentiating w.r.t. $\boldsymbol{\delta}_k$:

$$0 = \mathbf{g}_k + \mathbf{h}_k \boldsymbol{\delta}_k + \sqrt{\frac{3\boldsymbol{\rho}_k}{2\pi}} \text{sign}(\boldsymbol{\delta}_k) |\boldsymbol{\delta}_k|^{1/2}.$$

To enforce gradient descent, let $\boldsymbol{\delta}_k = -\text{sign}(\mathbf{g}_k) x^2$ and take $x > 0$. Substituting $\hat{\mathbf{h}}_k$, we can obtain the expression

$$0 = -\sqrt{\frac{|\mathbf{g}_k|}{2}} + \sqrt{\hat{\mathbf{h}}_k} x + \frac{\mathbf{h}_k}{\sqrt{2|\mathbf{g}_k|}} x^2.$$

The quadratic formula, keeping $x > 0$, gives

$$x = \frac{-\sqrt{\hat{\mathbf{h}}_k} + \sqrt{\hat{\mathbf{h}}_k + 2\mathbf{h}_k}}{\mathbf{h}_k \sqrt{\frac{2}{|\mathbf{g}_k|}}} = \frac{\sqrt{2|\mathbf{g}_k|}}{\sqrt{\hat{\mathbf{h}}_k} + \sqrt{\hat{\mathbf{h}}_k + 2\mathbf{h}_k}}$$

Substitution into $\boldsymbol{\delta}_k$ yields the stated result \blacksquare .

Proof of Theorem 6 The first claim easily follows by unpacking Equation (10) into Equation (13):

$$\mathbf{g}(\boldsymbol{\mu}^{(s+1)}) = \mathbf{g}^{(s)} + \varphi \bar{\mathbf{h}} * \boldsymbol{\delta}^{(s)} = (1 - \varphi) \mathbf{g}^{(s)} = \beta_1 \mathbf{g}^{(s)}.$$

Substituting the new gradient evaluation into Equation (14), using the error expression at step s from Equation (16), and placing the result in Equation (11) gives

$$\begin{aligned} \mathbf{g}^{(s+1)} &= \beta_1 \mathbf{g}^{(s)} + (1 - \beta_1) \left(\mathbf{g}^{(s)} - \boldsymbol{\gamma} + \boldsymbol{\omega} \mathbf{H} \boldsymbol{\delta}^{(s)} \right) \\ &= \left[\mathbf{g}^{(s)} - \boldsymbol{\gamma} \right] + \varphi \mathbf{H} \boldsymbol{\delta}^{(s)} + \beta_1 \boldsymbol{\gamma} = \mathbf{g}^*(\boldsymbol{\mu}^{(s+1)}) + \beta_1 \boldsymbol{\gamma} \blacksquare \end{aligned}$$

Algorithm 2: Alice Topography Update, Full Version

Input: evaluation center: ν ; gradient function: $g(\theta)$.**Input and Output:** Averages: $g, \rho, h_{\text{abs}}, h_{\text{rms}}^2$, and s .**Hyperparameters:** $\lambda, \beta_1, \beta_2$.This construction uses Equations (17) to (21) to adapt Theorems 1 to 3 with only one parameter-length temporary t .

- 1: Draw Rademacher t . Set parameters $\theta \leftarrow \nu + \lambda t$.
 - 2: Evaluate $g(\theta) = g^{(+)}$.
 - 3: Set parameters $\theta \leftarrow \nu - \lambda t$. Store $t \leftarrow g^{(-)}$.
 - 4: Evaluate $g(\theta) = g^{(-)}$.
 - 5: Update $h_{\text{abs}} \leftarrow \beta_2 h_{\text{abs}} + (1 - \beta_2) \frac{1}{2\lambda} |t - g^{(-)}|$.
 - 6: Update $h_{\text{rms}}^2 \leftarrow \beta_2 h_{\text{rms}}^2 + (1 - \beta_2) \frac{1}{4\lambda^2} (t - g^{(-)})^2$.
 - 7: Store $t \leftarrow \frac{1}{2}(t + g^{(-)})$. Set parameters $\theta \leftarrow \mu$.
 - 8: Evaluate $g(\theta) = g^{(0)}$.
 - 9: Update $g \leftarrow \beta_1 g + (1 - \beta_1) g^{(0)}$.
 - 10: Update $\rho \leftarrow \beta_2 \rho + (1 - \beta_2) \frac{2}{\lambda} (t - g^{(0)})^2$.
 - 11: Update $s \leftarrow \beta_2 s + (1 - \beta_2) g^{(0)2}$.
-

B Methodological Details

Restricted Updates: When a perturbation contains a relatively small value of $|\delta_i|$, the corresponding element of the matrix-vector product y_i expresses only a small contribution from the diagonal m_i . With this in mind, we observe the variance of the diagonal estimator can be further reduced by rejecting updates to a running m_i estimate from samples with $|\delta_i|$ below a threshold λ_{\min} . The reason an improvement is possible is because these rejections change the active density from $p(\delta_i)$ to a restricted density

$$r(\delta_i) \propto \begin{cases} p(\delta_i) & |\delta_i| \geq \lambda_{\min} \\ 0 & \text{otherwise.} \end{cases}$$

For example, if we average s standard normal samples and set $\omega_i^2 = 1$, then Theorem 2 gives

$$\kappa_i^*(\delta_i) = \frac{2\delta_i}{\delta_i^2 + 1} \quad \text{with variance} \quad V = \frac{3}{s} m_i^2.$$

Here, we have divided the single-sample variance by the number of samples. By sampling from the same distribution, but only updating if $|\delta_i| \geq 1$, the optimal kernel becomes:

$$\kappa_i^*(\delta_i) = \frac{1.40\delta_i}{\delta_i^2 + 1} \quad \text{with} \quad V = \frac{0.823}{0.317s} m_i^2 = \frac{2.60}{s} m_i^2.$$

Note the reduction in effective samples to account for the update probability: 31.7%. Nevertheless, these restricted updates improve the combined result.

Algorithms: Algorithm 2 shows the full topography update computations used by Alice in a formulation that only requires one additional parameter-length temporary variable. Alice also enables an RMS Hessian approximation shown in Algorithm 2, Line 6. Taking the square root of the running second moment yields a non-negative approximation that is suitable for QN steps. This approach is similar

Algorithm 3: Alice Optimization Step

Input: running averages: g, ρ, h , and s .**Input and Output:** parameters: μ .**Output:** evaluation center: ν .**Hyperparameters:** limit-method, $\lambda, \lambda_{\min}, \lambda_{\max}, \varepsilon$.

These parameter updates enable Theorems 4 to 6 while controlling exploitation stability with Adam-based limits.

- 1: Compute glass term, $\hat{h} = \frac{3}{4\pi} \rho * (|g| + \varepsilon)^{-1}$, and
 - 2: modified Hessian, $\bar{h} = \hat{h} + h + \sqrt{\hat{h} * (\hat{h} + 2h)} + \varepsilon$.
 - 3: Get quasi-Newton scale, $\delta = |g| * \bar{h}^{-1}$, and
 - 4: Fixed scale limits, $\delta_{\min/\max} = \lambda_{\min/\max}$; or
 - 5: SGD-M limits, $\delta_{\min/\max} = \lambda_{\min/\max} |g|$; or
 - 6: Adam limits, $\delta_{\min/\max} = \lambda_{\min/\max} |g| * (\sqrt{s} + \varepsilon)^{-1}$.
 - 7: Enforce bounds, $\delta \leftarrow \max(\delta_{\min}, \min(\delta_{\max}, \delta))$.
 - 8: Correct the sign for descent, $\delta \leftarrow -\text{sign}(g)\delta$.
 - 9: Update evaluation center, $\nu \leftarrow \mu + \omega\delta$.
 - 10: Update parameters, $\mu \leftarrow \mu + \varphi\delta$.
-

to that of AdaHessian (Yao et al. 2021), except they average results over parameter blocks.

Algorithm 3 shows the modified quasi-Newton steps for both glass density ρ and a Hessian diagonal h , but either term can be set to zero in practice. Then, the Adam factor and step bounds are applied before correcting the sign for gradient descent.

C Experimental Setup

Our experiments leverage existing benchmarks and we report the minimum, median, and maximum relevant outcomes for each case. Not only does this express the full range of outcomes, it also indicate the best quality model that would be used in practice.

Hardware and Software Tests are performed on compute nodes that each contain AMD 32-core CPUs and 1 NVidia A100 GPU with 40GB of memory. Software is written for PyTorch 2.2.1 with Cuda 11.8 drivers.

ResNet18, Power Law: The results in Figure 1 are generated with a specialized version of Alice that uses extra memory and gradient evaluations to compute and store gradient variations at λ and 2λ . Training is performed on a modified version of ResNet18 with multiplicative masks on channels, which improves prediction quality for SGDM, Adam, and Alice. We train for 40 epochs using $\lambda = 0.002, \beta_1 = 0.9, \beta_2 = 0.999, \varepsilon = 10^{-8}, \varphi = 0.1, \omega = 1.0, \lambda_{\min} = 0, \lambda_{\max} = 0.002, \text{quick_steps} = 0$, and Adam-based limiting. Step curvature uses both ρ and h_{abs} .

ResNet18, NAQ: The ResNet18 trials in Figure 4 use the same settings as above, except with the tuned learning rate of $\lambda = 0.005$, fixed-scale limiting with $\lambda_{\max} = 0.005$, and trained for 60 epochs. These options were tuned from the set $\{0.001, 0.002, 0.005, 0.01, 0.02, 0.05\}$ and trying both Adam-based limiting and fixed scale limiting with $\lambda_{\max} = \lambda$ or $\lambda_{\max} = 2\lambda$. Results include 10 seeds.

Settings			Test Accuracy		
φ	ω	Terms	Min	Median	Max
1.0	1.0	ρ	90.6%	91.2%	91.5%
1.0	1.0	h_{abs}	89.7%	90.1%	90.8%
1.0	1.0	$\rho + h_{\text{abs}}$	91.0%	91.8%	92.7%
1.0	1.0	h_{rms}	90.5%	90.8%	91.2%
0.1	1.0	ρ	92.1%	92.6%	92.7%
0.1	1.0	h_{abs}	91.8%	91.9%	92.1%
0.1	1.0	$\rho + h_{\text{abs}}$	92.1%	92.4%	92.8%
0.1	1.0	h_{rms}	91.8%	92.3%	92.7%

ViT, NAQ: Our vision transformer trials in Figure 4 use 8 encoding layers based on a linear-complexity attention formulation (Shen et al. 2021) and trained with the 64×64 downsampled Imagenet (Deng et al. 2009; Chrabaszcz, Loshchilov, and Hutter 2017). We train for 4 epochs using $\lambda = 0.005$, $\beta_1 = 0.9$, $\beta_2 = 0.999$, $\varepsilon = 10^{-8}$, $\lambda_{\text{min}} = 0$, $\lambda_{\text{max}} = 0.01$, $\text{quick_steps} = 3$, and Adam-based limiting. Results include 5 seeds.

Settings			Test Loss		
φ	ω	Terms	Min	Median	Max
1.0	1.0	ρ	4.49	4.49	4.55
1.0	1.0	h_{abs}	4.45	4.49	4.73
1.0	1.0	$\rho + h_{\text{abs}}$	4.41	4.48	4.48
1.0	1.0	h_{rms}	4.46	4.47	4.65
0.1	1.0	ρ	4.08	4.09	4.12
0.1	1.0	h_{abs}	4.13	4.13	4.14
0.1	1.0	$\rho + h_{\text{abs}}$	4.05	4.07	4.11
0.1	1.0	h_{rms}	4.14	4.15	4.15

Tensorized Transformer, Stability Limit: Our Tensorised Transformer trials use the architecture described by Ma et al. (2019), with a dropout rate of 0.1 and batch-size 60 for 50,000 steps. The results shown in Figure 5 are obtained from Alice with $\lambda = 0.001$, $\beta_1 = 0.9$, $\beta_2 = 0.999$, $\varepsilon = 10^{-8}$, $\varphi = 0.1$, $\omega = 1.0$, $\text{quick_steps} = 3$, and Adam-based limiting. Results include 10 seeds. It remains unclear why NAQ is not as effective as full quasi-Newton steps for this problem.

Settings		Validation PPL		
λ_{max}	Terms	Min	Median	Max
1.0×10^{-3}	ρ	40.4	43.2	49.1
1.0×10^{-3}	h_{abs}	38.6	43.7	47.1
1.0×10^{-3}	$\rho + h_{\text{abs}}$	39.8	45.1	48.2
1.0×10^{-3}	h_{rms}	39.4	42.9	51.2
2.5×10^{-3}	ρ	28.8	33.6	35.8
2.5×10^{-3}	h_{abs}	30.0	32.5	36.8
2.5×10^{-3}	$\rho + h_{\text{abs}}$	31.0	34.8	39.1
2.5×10^{-3}	h_{rms}	28.9	33.7	39.9

ResNet18, Training Methods: For ResNet18 results in Figure 6, the Adam trials use $\lambda = 0.001$, $\beta_1 = 0.9$, $\beta_2 = 0.999$, and $\varepsilon = 1E^{-8}$. SGD-M uses $\lambda = 0.001$ and $\beta = 0.9$. AdaHessian uses $\lambda = 0.15$, which gave the best results from the set $\lambda \in \{0.1, 0.15, 0.2, 0.25, 0.3\}$. Alice uses $\lambda = 5e-3$, $\beta_1 = 0.9$, $\beta_2 = 0.999$, $\varepsilon = 1E^{-8}$, $\varphi = 0.1$, $\omega = 1.0$, $\lambda_{\text{min}} = 0$, $\lambda_{\text{max}} = 0.01$, $\text{quick_steps} = 3$, and Adam-based limiting. Curvature includes both ρ and h_{abs} . Results include 30 seeds.

Method	Test Accuracy		
	Min	Median	Max
Adam	93.23%	93.41%	93.73%
SGDM	92.65%	93.19%	93.75%
AdaHessian	78.41%	90.25%	91.50%
Alice, $\rho + h_{\text{abs}}$	93.50%	93.76%	93.96%

Tensorised Transformer, Training Methods: The Tensorised Transformer results in Figure 6 use the same settings as above, but taking 200,000 steps. Adam and Alice use $\lambda = 0.00025$, $\beta_1 = 0.9$, $\beta_2 = 0.999$, and $\varepsilon = 1E^{-8}$, but Alice also includes $\varphi = 1.0$, $\omega = 1.0$, $\lambda_{\text{max}} = 0.000375$, $\text{quick_steps} = 1$, and Adam-based limiting. AdaHessian uses $\lambda = 0.00025$. Results include 5 seeds.

Method	Validation PPL		
	Min	Median	Max
Adam	20.84	21.83	21.86
AdaHessian	22.12	24.23	25.79
Alice, ρ	21.07	23.43	24.95
Alice, h_{abs}	18.66	21.50	23.74

Acknowledgments

Sandia National Laboratories is a multimission laboratory managed and operated by National Technology and Engineering Solutions of Sandia, LLC., a wholly owned subsidiary of Honeywell International, Inc., for the U.S. Department of Energy’s National Nuclear Security Administration under contract DE-NA-0003525. This paper describes objective technical results and analysis. Any subjective views or opinions that might be expressed in the paper do not necessarily represent the views of the U.S. Department of Energy or the United States Government.

We appreciate feedback during writing from Esha Datta, Connor Mattes, and Arvind Prasad that helped improve the clarity of this work.

References

- Becker, S.; Le Cun, Y.; et al. 1988. Improving the convergence of back-propagation learning with second order methods. In *Proceedings of the 1988 connectionist models summer school*, 29–37.
- Bottou, L.; Curtis, F. E.; and Nocedal, J. 2018. Optimization methods for large-scale machine learning. *SIAM review*, 60(2): 223–311.
- Choromanska, A.; Henaff, M.; Mathieu, M.; Arous, G. B.; and LeCun, Y. 2015. The loss surfaces of multilayer networks. In *Artificial intelligence and statistics*, 192–204. PMLR.
- Chrabaszcz, P.; Loshchilov, I.; and Hutter, F. 2017. A downsampled variant of imagenet as an alternative to the cifar datasets. *arXiv preprint arXiv:1707.08819*.
- Dauphin, Y. N.; Pascanu, R.; Gulcehre, C.; Cho, K.; Ganguli, S.; and Bengio, Y. 2014. Identifying and attacking the saddle point problem in high-dimensional non-convex optimization. *Advances in neural information processing systems*, 27.

- Deng, J.; Dong, W.; Socher, R.; Li, L.-J.; Li, K.; and Fei-Fei, L. 2009. Imagenet: A large-scale hierarchical image database. In *2009 IEEE conference on computer vision and pattern recognition*, 248–255. Ieee.
- Duersch, J. A. 2024. Projective Integral Updates for High-Dimensional Variational Inference. *SIAM/ASA Journal on Uncertainty Quantification*, 12(1): 69–100.
- Frumkin, N.; Gope, D.; and Marculescu, D. 2023. Jumping through local minima: Quantization in the loss landscape of vision transformers. In *Proceedings of the IEEE/CVF International Conference on Computer Vision*, 16978–16988.
- He, K.; Zhang, X.; Ren, S.; and Sun, J. 2016. Deep residual learning for image recognition. In *Proceedings of the IEEE conference on computer vision and pattern recognition*, 770–778.
- Hemati, S.; Zhang, G.; Estiri, A.; and Chen, X. 2023. Understanding hessian alignment for domain generalization. In *Proceedings of the IEEE/CVF International Conference on Computer Vision*, 19004–19014.
- Indrapriyadarsini, S.; Mahboubi, S.; Ninomiya, H.; and Asai, H. 2020. A stochastic quasi-newton method with nesterov’s accelerated gradient. In *Machine Learning and Knowledge Discovery in Databases: European Conference, ECML PKDD 2019, Würzburg, Germany, September 16–20, 2019, Proceedings, Part I*, 743–760. Springer.
- Kaur, S.; Cohen, J.; and Lipton, Z. C. 2023. On the maximum hessian eigenvalue and generalization. In *Proceedings of Machine Learning Research*, 51–65. PMLR.
- Kingma, D. P.; and Ba, J. 2014. Adam: A method for stochastic optimization. *arXiv preprint arXiv:1412.6980*.
- Kong, Y.; Liu, L.; Chen, H.; Kacprzyk, J.; and Tao, D. 2023. Overcoming catastrophic forgetting in continual learning by exploring eigenvalues of Hessian matrix. *IEEE Transactions on Neural Networks and Learning Systems*.
- Krizhevsky, A.; and Hinton, G. 2009. Learning multiple layers of features from tiny images. Technical report, Citeseer.
- LeCun, Y.; Denker, J.; and Solla, S. 1989. Optimal brain damage. *Advances in neural information processing systems*, 2.
- Lee, J.; Yoo, J.; and Kwak, N. 2023. SHOT: suppressing the hessian along the optimization trajectory for gradient-based meta-learning. *Advances in Neural Information Processing Systems*, 36: 61450–61465.
- Lee, S.; He, C.; and Avestimehr, S. 2023. Achieving small-batch accuracy with large-batch scalability via Hessian-aware learning rate adjustment. *Neural Networks*, 158: 1–14.
- Li, L.; and Spratling, M. 2023. Understanding and combating robust overfitting via input loss landscape analysis and regularization. *Pattern Recognition*, 136: 109229.
- Li, X.-C.; Li, L.; and Zhan, D.-C. 2024. Visualizing, Rethinking, and Mining the Loss Landscape of Deep Neural Networks. *arXiv preprint arXiv:2405.12493*.
- Lyle, C.; Zheng, Z.; Nikishin, E.; Pires, B. A.; Pascanu, R.; and Dabney, W. 2023. Understanding plasticity in neural networks. In *International Conference on Machine Learning*, 23190–23211. PMLR.
- Ma, X.; Zhang, P.; Zhang, S.; Duan, N.; Hou, Y.; Zhou, M.; and Song, D. 2019. A tensorized transformer for language modeling. *Advances in neural information processing systems*, 32.
- Merity, S.; Xiong, C.; Bradbury, J.; and Socher, R. 2016. Pointer sentinel mixture models. *arXiv preprint arXiv:1609.07843*.
- Nair, V.; and Hinton, G. E. 2010. Rectified linear units improve restricted boltzmann machines. In *Proceedings of the 27th international conference on machine learning (ICML-10)*, 807–814.
- Ninomiya, H. 2017. A novel quasi-Newton-based optimization for neural network training incorporating Nesterov’s accelerated gradient. *Nonlinear Theory and Its Applications, IEICE*, 8(4): 289–301.
- Nocedal, J.; and Wright, S. J. 2006. Theory of constrained optimization. *Numerical optimization*, 304–354.
- Parisi, G. 2007. Course 3 Mean field theory of spin glasses: Statics and dynamics. *Les Houches*, 85: 131–178.
- Ruder, S. 2016. An overview of gradient descent optimization algorithms. *arXiv preprint arXiv:1609.04747*.
- Sen, M.; Mohan, C. K.; and Qin, A. K. 2023. Federated Optimization with Linear-Time Approximated Hessian Diagonal. In *International Conference on Pattern Recognition and Machine Intelligence*, 106–113. Springer.
- Shen, Z.; Zhang, M.; Zhao, H.; Yi, S.; and Li, H. 2021. Efficient attention: Attention with linear complexities. In *Proceedings of the IEEE/CVF winter conference on applications of computer vision*, 3531–3539.
- Spigler, S.; Geiger, M.; d’Ascoli, S.; Sagun, L.; Biroli, G.; and Wyart, M. 2019. A jamming transition from under- to over-parametrization affects generalization in deep learning. *Journal of Physics A: Mathematical and Theoretical*, 52(47): 474001.
- Yao, Z.; Gholami, A.; Keutzer, K.; and Mahoney, M. W. 2020. Pyhessian: Neural networks through the lens of the hessian. In *2020 IEEE international conference on big data (Big data)*, 581–590. IEEE.
- Yao, Z.; Gholami, A.; Shen, S.; Mustafa, M.; Keutzer, K.; and Mahoney, M. 2021. Adahessian: An adaptive second order optimizer for machine learning. In *proceedings of the AAAI conference on artificial intelligence*, volume 35, 10665–10673.